TU Delft

Delft University of Technology

Numerical simulation of a flapping micro aerial vehicle through wing deformation capture

Tay, W. B.; De Baar, J. H.S.; Percin, M.; Deng, S.; Van Oudheusden, B. W.

DOI
10.2514/1.J056482

Publication date
2018

Document Version
Final published version

Published in
AIAA Journal

Citation (APA)
Tay, W. B., De Baar, J. H. S., Percin, M., Deng, S., & Van Oudheusden, B. W. (2018). Numerical simulation of a flapping micro aerial vehicle through wing deformation capture. *AIAA Journal*, *56*(8), 3257-3270. https://doi.org/10.2514/1.J056482

Important note
To cite this publication, please use the final published version (if applicable).
Please check the document version above.

Copyright
Other than for strictly personal use, it is not permitted to download, forward or distribute the text or part of it, without the consent of the author(s) and/or copyright holder(s), unless the work is under an open content license such as Creative Commons.

Takedown policy
Please contact us and provide details if you believe this document breaches copyrights.
We will remove access to the work immediately and investigate your claim.

This work is downloaded from Delft University of Technology.
For technical reasons the number of authors shown on this cover page is limited to a maximum of 10.

Green Open Access added to TU Delft Institutional Repository

'You share, we take care!' - Taverne project

https://www.openaccess.nl/en/you-share-we-take-care

Otherwise as indicated in the copyright section: the publisher is the copyright holder of this work and the author uses the Dutch legislation to make this work public.

AIAA JOURNAL
Vol. 56, No. 8, August 2018

Numerical Simulation of a Flapping Micro Aerial Vehicle Through Wing Deformation Capture

W. B. Tay*
National University of Singapore, Singapore 117411, Republic of Singapore
J. H. S. de Baar†
University of New South Wales Canberra, Campbell, Australian Capital Territory 2612, Australia
M. Percin‡
Middle East Technical University, 06800 Ankara, Turkey
S. Deng§
Northwestern Polytechnical University, 710072 Xi'an, People's Republic of China
and
B. W. van Oudheusden¶
Delft University of Technology, 2629 HS Delft, The Netherlands

DOI: 10.2514/1.J056482

Three-dimensional numerical simulations of a four-wing flapping micro aerial vehicle (FMAV) with actual experimentally captured wing membrane kinematics have been performed using an immersed boundary method Navier–Stokes finite volume solver. To successfully simulate the clap and fling motion involving the wing intersection, the numerical solver has been specifically modified to use a newly improved interpolation template searching algorithm to prevent divergence. Reasonable agreement was found between the numerical and experimental results, with the first and second force peaks from the experimental results well captured by the simulations, which was not possible in the past. Moreover, a "V-shaped linked" vortex was observed, which was similar to the vortical structures found in other experiments and simulations. A wing drag analysis showed that the drag magnitude of the clap and fling configuration was about 2.5 times that of the single-wing configuration. Visualizations of the flowfields through pressure contours and vortical isosurfaces led to a better understanding of the underlying flapping-wing aerodynamics. The ability to accurately simulate the FMAV with flexible wings opened up many opportunities for further FMAV design-related problems.

Downloaded by TU DELFT on October 22, 2020 | http://arc.aiaa.org | DOI: 10.2514/1.J056482

Nomenclature

c	=	mean chord length of wing (wing area/wing span)
c_d	=	drag coefficient
c_l	=	lift coefficient
c_t	=	thrust coefficient
c_x	=	force coefficient along the positive x direction
c_y	=	force coefficient along the positive y direction
dx	=	minimum grid size
F_i	=	nondimensional force along the positive i direction
f	=	actual flapping frequency
fc	=	external body force
k	=	reduced frequency (fc/U_{ref})
p	=	pressure
Q	=	Q criterion
Re	=	Reynolds number ($(U_{\text{ref}} \times c)$/kinematic viscosity of air)
S	=	wing surface area
T	=	flapping period
t	=	time, nondimensionalized with the flapping period
U_{ref}	=	reference velocity (taken as the average wing tip velocity)
θ	=	angle of the leading edge of the wing made with the positive y axis

Presented as Paper 2016-3552 at the 34th AIAA Applied Aerodynamics Conference, Washington, D.C., 13–17 June 2016; received 29 June 2017; revision received 16 February 2018; accepted for publication 2 April 2018; published online 29 June 2018. Copyright © 2018 by W. B. Tay. Published by the American Institute of Aeronautics and Astronautics, Inc., with permission. All requests for copying and permission to reprint should be submitted to CCC at www.copyright.com; employ the ISSN 0001-1452 (print) or 1533-385X (online) to initiate your request. See also AIAA Rights and Permissions www.aiaa.org/randp.

*Research Scientist, Temasek Laboratories, 5A Engineering Drive 1; tsltaywb@nus.edu.sg.

†Research Associate, School of Engineering and Information Technology, Northcott Dr.; j.debaar@adfa.edu.au. Member AIAA.

‡Assistant Professor, Department of Aerospace Engineering, Faculty of Engineering, Çankaya; Faculty of Aerospace Engineering, Delft University of Technology, Kluyverweg 1, 2629 HS Delft, The Netherlands; mpercin@metu.edu.tr. Member AIAA.

§Associate Professor, School of Power and Energy, Youyi West Road 127; Faculty of Aerospace Engineering, Delft University of Technology, Kluyverweg 1, 2629 HS Delft, The Netherlands; s.deng@nwpu.edu.cn. Member AIAA.

¶Associate Professor, Faculty of Aerospace Engineering, Kluyverweg 1; b.w.vanoudheusden@tudelft.nl.

I. Introduction

THERE are currently several different types of flapping micro aerial vehicles (FMAVs) available. Some of these include the DelFly [1] (a forward-flying FMAV with two pairs of wings, developed by the Delft University of Technology), the hybrid fixed/flapping-wing micro aerial vehicle (MAV) [2] (a hovering FMAV that has one pair of flapping wings and one pair of fixed wings, developed by Temasek Laboratories of the National University of Singapore), and the nano-hummingbird [3] (a flapping MAV with a single pair of wings, developed by AeroVironment). Due to the severe weight constraints, they need to be made as light as possible, and therefore usually feature relatively complex geometrical construction with membrane-based wings. Due to the unsteady wing kinematics and the flexible membrane wing, the aerodynamics of the flowfields involved are very complex. To achieve a better understanding of the FMAV flight characteristics, experiments involving particle image velocimetry (PIV) can be used to visualize the velocity flowfield or vorticity plots [4]. However, this is a time-consuming and laborious task. Moreover, due to the limitation of the apparatus and experimental setup, it is generally not possible to obtain a complete characterization of the flowfields, especially in the wing vicinity due to laser reflection, as mentioned in the work by Groen et al. [5]. The difficulty increases when there is more than one wing, such as in a clap and fling motion, as described by Weis-Fogh

Downloaded by TU DELFT on October 22, 2020 | http://arc.aiaa.org | DOI: 10.2514/1.J056482

[6], where the wings come into close contact with one another. Without a full picture, it may not be possible to explain the underlying aerodynamics happening in the wing's vicinity. Lastly, compared to numerical simulations, the temporal and spatial resolution of PIV is usually lower and some important information may be lost in the process, as mentioned by Garmann et al. [7].

An alternative or additional approach for the aerodynamic analysis of an FMAV is through the use of numerical flow simulations. To perform a realistic simulation of the phenomenon, it is required to have a numerical solver that is capable of handling fluid–structure interaction (FSI) because the wings deform significantly during flapping. Almost all current FMAVs use thin membrane material such as Mylar as their wings. Simulating the thin and flexible membrane wing is a nontrivial task because the wing deformation is highly nonlinear. There are many parameters involved, and it is computationally expensive because the structural solver must be coupled with the fluid solver. For an accurate and stable simulation, it is also recommended to perform twoway coupled or inner iterations. Tian et al. [8] used a three-dimensional (3-D) numerical solver with a nonlinear finite element solid-mechanics solver for the FSI simulation of the cicada and its wings. The authors reported that accurate and efficient numerical approaches for modeling large flexible-wing deformations were still scarce. Similarly, Nakata and Liu [9] also performed FSI simulation on the hawk moth's wing.

An appealing alternative methodology is to use an optical tracking procedure to determine the FMAV wing motion and deformation, and then use the wing shape captured as an input to the numerical solver. This will allow one to perform a realistic simulation of the FMAV, without needing to model the structural dynamics, as required in a true FSI simulation. Viswanath et al. [10] used the bat's wing deformation data (supplied by Riskin et al. [11]) to obtain the force coefficients and flowfields of a bat's climbing flight. Nakata et al. [12] used a similar technique in their FMAV simulations. Deng et al. [13] recently performed a study that validated the accuracy of the FMAV membrane wing capture qualitative and quantitative results with numerical results. In the numerical experimental thrust comparison of the DelFly, there is good agreement for the peak thrust during the instroke. However, the peak thrust predicted numerically is lower than the experimental prediction during the outstroke. The authors attribute the discrepancy to the minimum clearance that must be applied to ensure the stability of the simulation. In the experiment, the wings briefly touch one another.

The objective of this study is therefore to perform a validation between the FMAV experimental thrust and the numerical simulation results. The wing kinematics in the simulations use the experimentally determined wing deformation data. An immersed boundary method (IBM) [14] 3-D Navier–Stokes solver will be used. Improvements are made to the solver with respect to its previous version by Tay et al. [15], which allow it to handle wings in close contact and even intersections. This crucial feature is not found in other numerical solvers, such as those by Nakata et al. [12] and Deng et al. [13]. This is especially important in this scenario because our FMAV exhibits a clap and fling motion, as described by Lighthill [16]. The flowfields around the wings will be visualized by means of pressure/vorticity contour plots, and they will be analyzed. It is expected that the results obtained from this study will further enhance the understanding of the aerodynamic behavior of the FMAV and, as such, be beneficial to their further improvement. In perspective, it could, for example, pave the way for future related studies such as wind gust or tail effect.

II. Experimental Setup

This section describes procedures that were followed to obtain the raw wing deformation data. More details about the experimental procedures can be found in the work by Percin et al. [17]. The FMAV of interest is the DelFly II (hereafter referred to as the DelFly for short): an FMAV that has been developed by the Delft University of Technology [1,18], as shown in Figs. 1a and 1b [19]. It has two pairs of wings that undergo counterphase flapping. Its wingspan is 0.28 m, and it weighs about 16 g without an onboard sensor. It was chosen as the test platform for the current investigation because it has been the subject of much of the previous research [5,18,20], making it a proven and well-tested configuration. The outline of the wing of the DelFly is shown in Fig. 2a. The leading edge is attached to a carbon rod (represented by the thick horizontal black line), which makes it relatively rigid in the spanwise direction. The root chord edge is fixed and not allowed to deform. On the other hand, the tip chord and trailing edge are free to deform. Blue dot markers (a total of 200) are added to one wing to allow the camera system to track the wing surface deformation. However, the innermost two lines are omitted due to the loss of some markers in the images, resulting in 166 dots being processed. The experimental setup is shown in Fig. 2b, where the red circle indicates the DelFly's position and the blue arrows show the camera light rays' directions. We use three high-speed cameras: two of which form the stereovision system that tracks the markers on the wing, whereas the third one is positioned in a front view to capture the leading edges and determine the phase of the motion. The measurement volume is calibrated by scanning a three-dimensional target plate through the volume with a depth of 140 mm and steps of 20 mm. The calibration information is acquired by use of the PIV software LaVision Davis 8.1.6. Automation in the detection of the markers is facilitated by the use of a structured grid of markers. The detailed procedure can be found in the work by Percin et al. [17]. Then, an in-house MATLAB code is used to determine the three-dimensional coordinates of the marker positions. One-thousand images are recorded at a framing frequency of 1 kHz. With regard to force measurements, the DelFly is attached to the ATI Nano17 titanium force sensor to record the thrust generated by its wings. The thrust is initially denoised by a zero-shift Chebyshev II low-pass filter to get rid of the structural vibration effects. It is then filtered with a cutoff frequency at 2.5 times the flapping frequency to remove noise from the experimental data because additional tests carried out under near-vacuum conditions, as described by Percin et al. [17], showed that only the first two harmonics were associated with aerodynamic



a) b)

Fig. 1 DelFly [19] views: a) isometric and b) side.

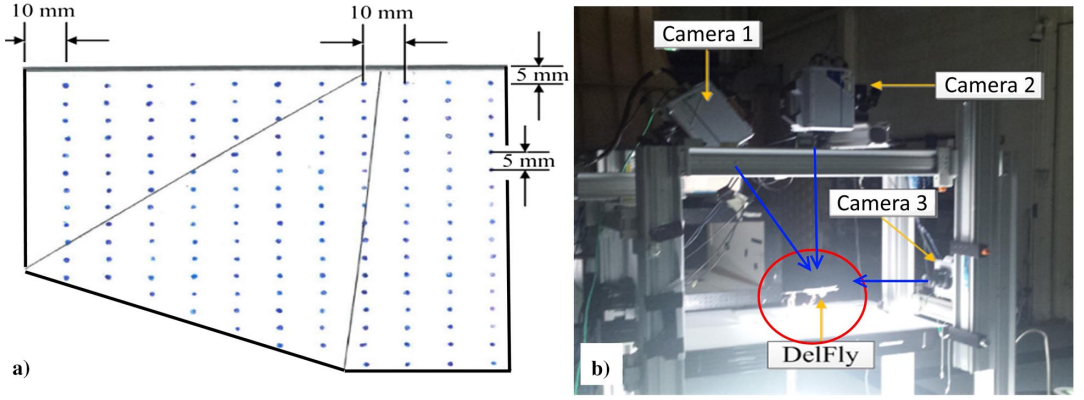


Fig. 2 Representations of a) DelFly wing with dots; and b) experimental setup for the wing deformation capture, adapted from the work of Deng et al. [13].

forces. [Although only the first two harmonics are associated with aerodynamic forces, we choose the cutoff frequency at 2.5 times the flapping frequency (20 Hz). This is because, if two times the flapping frequency is used, there is a high chance of influencing the second force data peak due to the ripples or the transition band of the filter. Therefore, it is always more appropriate to define the cutoff frequency slightly higher than the peak frequency we want to preserve. The same principle is applied to the higher cutoff frequencies as well.] However, to have a more complete picture of the problem, we also filter the force data with the cutoff frequencies at 3.5, 8.5, 9.5, and 10.5 times the flapping frequency. These force data will be used to validate the accuracy of the simulation results, and the comparison with different cutoff frequencies will be discussed.

Out of the four DelFly wings, note that only one wing has dots, and hence the deformation was only captured on one wing in view of the inherent symmetry of the flapping mechanism along with the dihedral plane and fuselage. Our assumption is based on the fact that the design of the gearbox and wing is such that the wings are flapping at similar speeds, and hence exhibit similar flexibility. Some additional steps are required before the full four wings of the DelFly can be realized. These steps will be elaborated on in the research methodology section.

There are a number of problems associated with the acquisition of the wing deformation data. One of the problems is the loss of points in successive timeframes. Some points cannot be detected due to blockage or poor viewing angles of one of the two cameras in the measurements. The solution is to manually detect the points. In other words, the user must manually click on the points to record their 3-D coordinates using the in-house MATLAB code. This is, of course, much more tedious. The next problem involves the accuracy of the captured dots' locations. A minor discrepancy between the actual and calculated locations will be magnified during the derivation of the velocities and accelerations, which are required in the numerical solver. These errors can create spikes that cause the solver to diverge. Lastly, the captured wing appears "wavy" while flapping. In other words, it displays some vibrations as it flaps and deforms. This could be attributed to the high-speed deformation of the wing or the "noise" associated with the accuracy of the captured dots' locations. These issues are resolved or minimized using the kriging interpolation [21–23], which will be described in the research methodology section (Sec. IV).

III. Numerical Method

A. Solver

The solver used in this study is a three-dimensional immersed boundary method Navier–Stokes solver. The wings of the FMAV undergo large motions and deformations; the wings also touch and intersect one another briefly during the clap and fling event. It may be difficult and almost impossible to use an arbitrary Lagrangian–Eulerian formulation under these situations, which motivates our choice of using the IBM approach. Moreover, improvements have been made to the current solver to improve its stability, especially when the wings are in close vicinity or intersection occurs. Details about the improvements will be given in the next section.

In the IBM, stationary Cartesian grids are used and the body of interest simply cuts through the grid. We simulate the presence of the body by adding a forcing term fc to the Navier–Stokes momentum equation, as shown in Eq. (1):

$$\frac{\partial u}{\partial t} = -u \cdot \nabla u + \frac{1}{Re}\nabla^2 u - \nabla p + fc \tag{1}$$

where $\boldsymbol{u}$ is the velocity vector, t is the time, p is the pressure, and Re is the Reynolds number. Equation (1) has been nondimensionalized using the average wing tip velocity U_{ref} and mean chord length c as the reference velocity and length, respectively. Accordingly, the calculation of the Reynolds number Re is based on U_{ref} and c.

We use the discrete forcing approach based on a combination of the methods developed by Yang and Balaras [24], Kim et al. [25], and Liao et al. [26] to calculate fc. In this case, fc is provisionally calculated explicitly using the first-order forward Euler and second-order Adams–Bashforth (AB2) schemes for the viscous and convective terms, respectively, to give the following:

$$fc^{n+1} = \frac{u_f - u^n}{\Delta t} + \left(\frac{3}{2}\nabla.(uu)^n - \frac{1}{2}\nabla.(uu)^{n-1}\right) - \left(\frac{\nabla^2 u}{Re}\right)^n + \nabla p^n \tag{2}$$

where n refers to the time step:

$$\nabla \cdot u = 0 \tag{3}$$

To solve the modified nondimensionalized incompressible Navier–Stokes equations [Eqs. (1) and (3)], we use the finite volume fractional step method, which is based on an improved projection method, as described by Kim and Choi [27].

We use the AB2 and second-order Crank–Nicolson discretization for the time integration of the convective and viscous terms, respectively. For the spatial derivatives, the convective and viscous terms are discretized using the second-order central differencing on a staggered grid. We solve Eqs. (1) and (3) using the fractional step method, whereby the momentum equation is first solved to obtain a non-divergence-free velocity field. Using this non-divergence-free velocity, the pressure field is solved using the Poisson equation, which in turn updates the velocity to be divergence free. The momentum and Poisson equations are solved using the open-source linear equation solvers portable, extensible toolkit for scientific computation [28] and high performance preconditioners [29], respectively. No turbulence model is added to the solver because the flow is still largely laminar. Moreover, at $Re = 8775$, there is no suitable turbulent model.

B. Improvements to the Solver

As mentioned earlier, in the current simulations, the wings undergo a clap and fling motion, which requires the wings to be in close

Downloaded by TU DELFT on October 22, 2020 | http://arc.aiaa.org | DOI: 10.2514/1.J056482

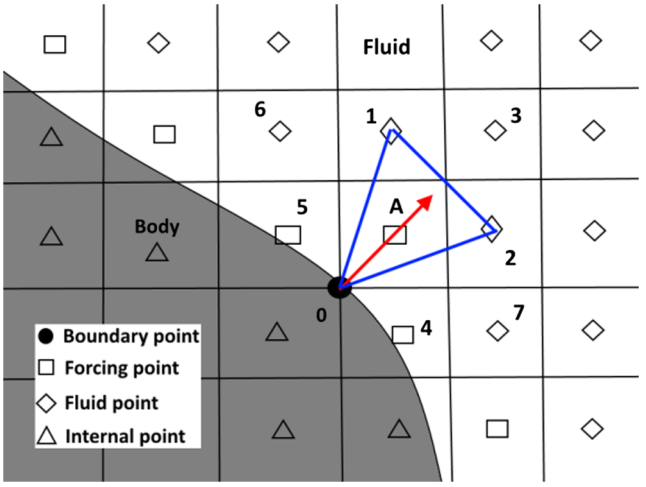


Fig. 3 Possible interpolation template for the forcing point.

contact and even to intersect. It will be difficult, if not impossible, for a grid-conforming solver to handle this situation. In the IBM, the bodies simply cut through the stationary Cartesian grid, so there is no grid quality issue. However, as reported by Tay et al. [15], there is a stability issue when the wings are close to one another, which causes the solution to diverge.

To improve the stability, we have made two modifications to the solver. The first improvement involves the optimized selection of the interpolation template. In the IBM, it is necessary to perform interpolation because the body interface does not coincide with the forcing points. We follow the interpolation template selection procedure by Yang and Balaras [24], as shown in two dimensions in Fig. 3. In this case, excluding compulsory boundary point 0, it is most ideal to choose fluid points 1 and 2 to form the triangle interpolation template for point A because they are nearest to point A. In fact, it is also possible to use any combinations of two additional points from 1 to 7 to form the template, although it is not ideal. In 3-D, one more fluid point is required and there are even more possible choices. To obtain the coefficients in 3-D, we assume that any variable ϕ can be expressed as follows:

$$\phi = a_1 + a_2 x + a_3 y + a_4 z \tag{4}$$

where the four unknowns a_1, a_2, a_3, and a_4 are the coefficients that can be obtained by solving four equations using three fluid points and one boundary point. Hence, this forms a well-determined system of equations.

To improve the solver's stability, we select the template such that the coefficients of the interpolation template should preferably be between zero and one, given that the sum of the coefficients is always one. In some cases, such as in the vicinity of the body's corners or when two bodies are in close contact, this is not possible. In these cases, we relax our criteria such that the maximum absolute coefficient is smaller than two. If this is still not possible, we switch to using the inverse distance weighing (IDW) by Shepard [30], which uses all possible surrounding points to construct the template. Using this interpolation method, the coefficients are always between zero and one. Based on past experience, using Eq. (4) gives better results in terms of accuracy, and hence it is the preferred choice before switching to IDW interpolation.

The second improvement involves using a boundary point from another body, which is in close contact with the current body, to form the interpolation template. As mentioned earlier, in the normal scenario, we only use one boundary point (point 0) from the nearest body to form the interpolation template. However, in the scenario whereby two bodies are in close contact, it is preferable to use a boundary point from another body as well, such that there is a total of two boundary points in the template. This also helps to improve the stability of the solver because boundary points contain known values through the prescribed motion of the bodies. Both modifications to the solver help to improve the stability of the solver and prevent divergence.

One concern of the solver involves the intersection of the bodies, which may at first appear nonphysical. However, we can imagine that the two bodies deform when they come together; hence, there is no intersection or "overlap" involved. An example of the change in the templates involved as two spheres come into collision is given in Fig. 4.

C. Force Calculations

As the body is not aligned with the Cartesian grid, we calculate the nondimensional force F_i on the body, using the forcing term fc^{n+1} obtained earlier, as described by Lee et al. [31]:

$$F_i = -\int_{\text{solid}} fc_i^{n+1}\,\mathrm{d}V + \int_{\text{solid}} \left(\frac{\partial u_i}{\partial t} + \frac{\partial u_i u_j}{\partial x_j}\right)\mathrm{d}V \tag{5}$$

where V is the volume of the wing.

The thrust coefficient c_t is then calculated using

$$c_t = \frac{2c^2 F_t}{S} \tag{6}$$

where c and S refer to the reference wing mean chord length and wing surface area, respectively.

D. Solver Validation

We have validated the IBM solver successfully against several experiments and other simulations. They include 1) the plunging wing experiment in a water tunnel at a Reynolds number Re of 10,000, which was performed by Calderon et al. [32]; 2) the symmetric rotation motion of a model fruit-fly-like wing in a water-tunnel experiment at a Reynolds number Re of 10,000, which was performed by Lua et al. [33]; and 3) wing deformation capture of the *Cynopterus brachyotis* fruit bat in forward flight by Viswanath et al. [34].

The force results between the first two experiments and simulations at the current resolution agree well. In the plunging wing

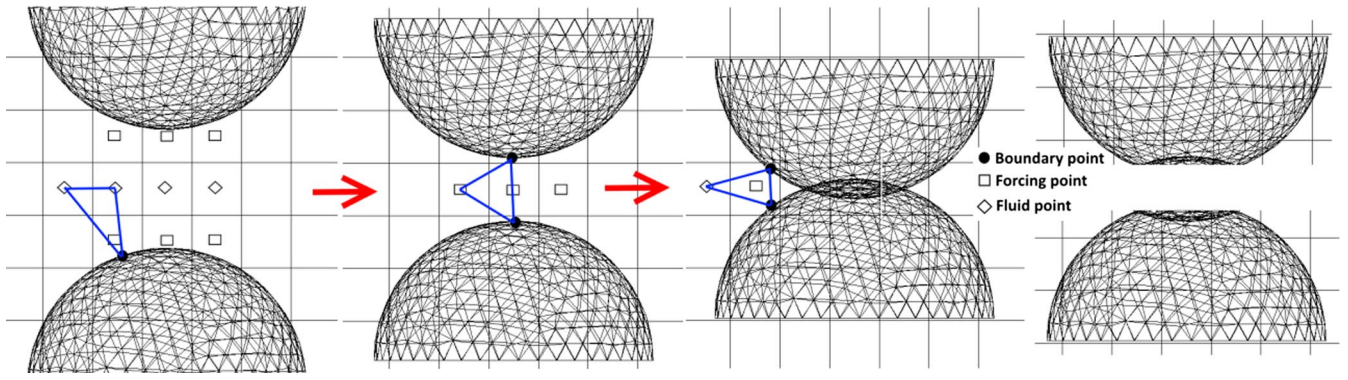


Fig. 4 Change in the templates involved as two spheres come into collision. The last diagram shows the deformed spheres as if there is no overlap involved.

Downloaded by TU DELFT on October 22, 2020 | http://arc.aiaa.org | DOI: 10.2514/1.J056482

experiment by Calderon et al. [32], the IBM solver predicted the trend of the forces correctly, although the magnitudes of the forces have been underpredicted. The IBM solver managed to capture the important vortex features of vorticity contour plots, although there were some minor differences. However, the other numerical solvers included in the comparison also underpredicted the forces and showed minor differences in the vorticity plots. In the model fruit-fly-like wing experiment by Lua et al. [33], the general shape and magnitude of the force graphs computed by the IBM solver compared well with the experimental results, except for some minor differences. More details about the comparison with the first two experiments can be found in the study by Tay et al. [35]. These validations confirmed that the IBM solver was able to accurately simulate moving wings up to $Re = 10{,}000$.

We have also simulated the forward flight of the fruit bat as obtained with wing deformation capture and compared our simulation results with that of Viswanath et al. (VT) [34]. The bat's flapping frequency and forward velocity were 1 Hz and 0.08 m/s, respectively, which corresponded to a Reynolds number Re of 433. Viswanath et al. also used an IBM solver for their simulations. As shown in Fig. 5, the comparisons for the c_t and c_l results were acceptable. s. It is difficult to comment on which solver gave the correct result because there were no experimental data for validation. However, some possible reasons for the different results included 1) the use of different interpolation schemes to update the position, velocity, and acceleration of the bat's wing during the simulation; 2) the use of different IBM schemes to evaluate the bat's wing surface

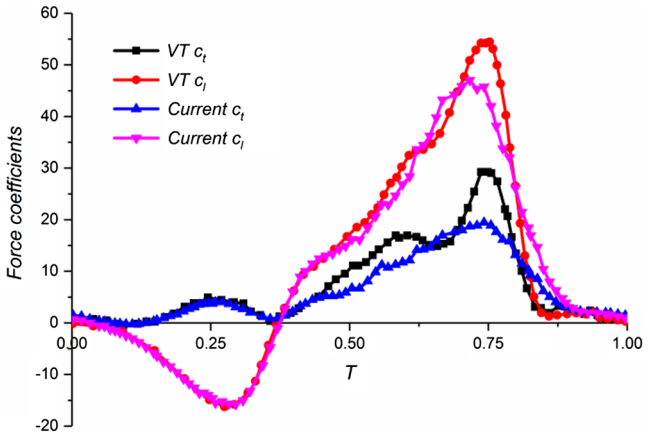


Fig. 5 Force coefficient comparison between the numerical solver of Viswanath et al. and the current IBM solver.

boundary condition; and 3) the use of different numerical schemes in each solver.

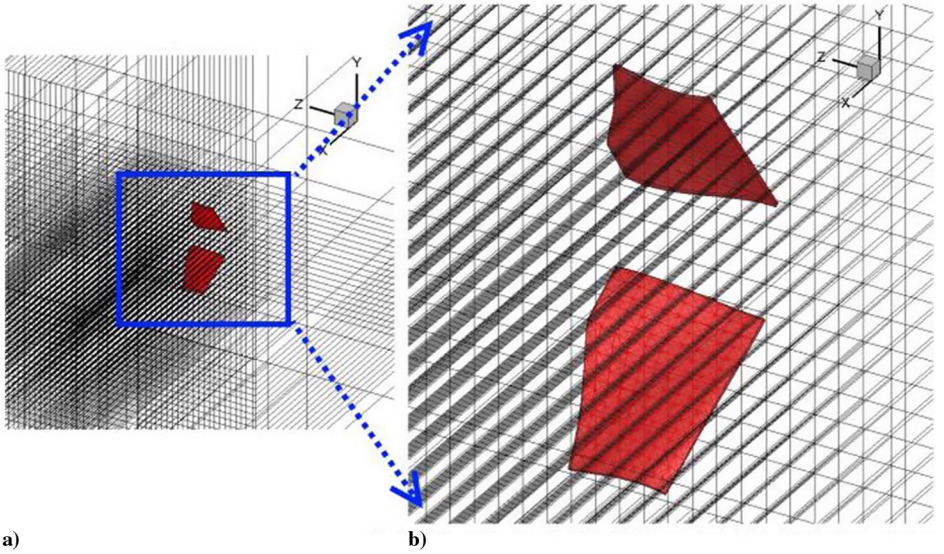
These modifications will increase the order and accuracy of our IBM solver. However, as mentioned earlier, an experimental validation is still essential. Nevertheless, the overall result comparison is still satisfactory between the two solvers. All the validations mentioned earlier were performed using the old IBM method. In those validations, there was no close body interaction or intersection. Hence, no special treatment was required and both the original and improved solver gave the same answer.

E. Simulation Setup and Grid Convergence Study

The IBM solver uses purely Cartesian grids. Similar to the design of the actual DelFly, which is flapping symmetrically in its left and right wings, we apply a symmetry boundary condition to the yz plane ($x = 0$) to mirror the other pair of wings to reduce the computational cost. The simulations are performed in quiescent flow, similar to the experimental setup. The computational domain is $10 \times 10 \times 21$ (in terms of nondimensional chord length c) in the x, y, and z directions, respectively, as shown in Fig. 6. A grid convergence study is performed using the kriging skip5 postprocessed wing, whereby the wing is postprocessed using kriging interpolation and data skip. More details about this wing are given in the methodology subsection (Sec. IV.A). Both the comparisons of c_t and c_l at different resolutions are shown in Fig. 7, but we can observe that the grid requirements for the thrust forces are higher than that of the lift. In other words, the thrust force is more sensitive to the changing grid resolutions. The results from Fig. 7 show that there are only small differences between the minimum grid lengths dx of $0.009c$, $0.012c$, and $0.018c$ in the peak region. We compute the rms values of the error of c_t for $0.036c$ to $0.012c$, assuming that $0.009c$ gives the exact solution. The results in Table 1 show that the error decreases with decreasing dx. Moreover, in Fig. 8 (where red circles indicate regions of differences in the pressure contours), there is greater similarity between $dx = 0.009c$ and $0.012c$ in the pressure contours. Hence, the minimum grid length of $0.012c$ will be used for all simulations in this study. Refinement is used in the region near the wings, and the resultant total number of cells for the domain is $226 \times 402 \times 410$. Running a case for three periods in parallel using 576 Intel® Xeon® CPU E5-2690 v3 processors at 2.60 GHz takes about 4 h.

IV. Research Methodology

The main objective of this study is twofold. First, we would like to perform a validation between the thrust produced by DelFly experimentally and numerically by using the captured wing deformation data. The difficulties of using this approach have been



a) b)

Fig. 6 Cartesian grid: a) normal and b) close-up isometric views, with the wings in red.

Downloaded by TU DELFT on October 22, 2020 | http://arc.aiaa.org | DOI: 10.2514/1.J056482

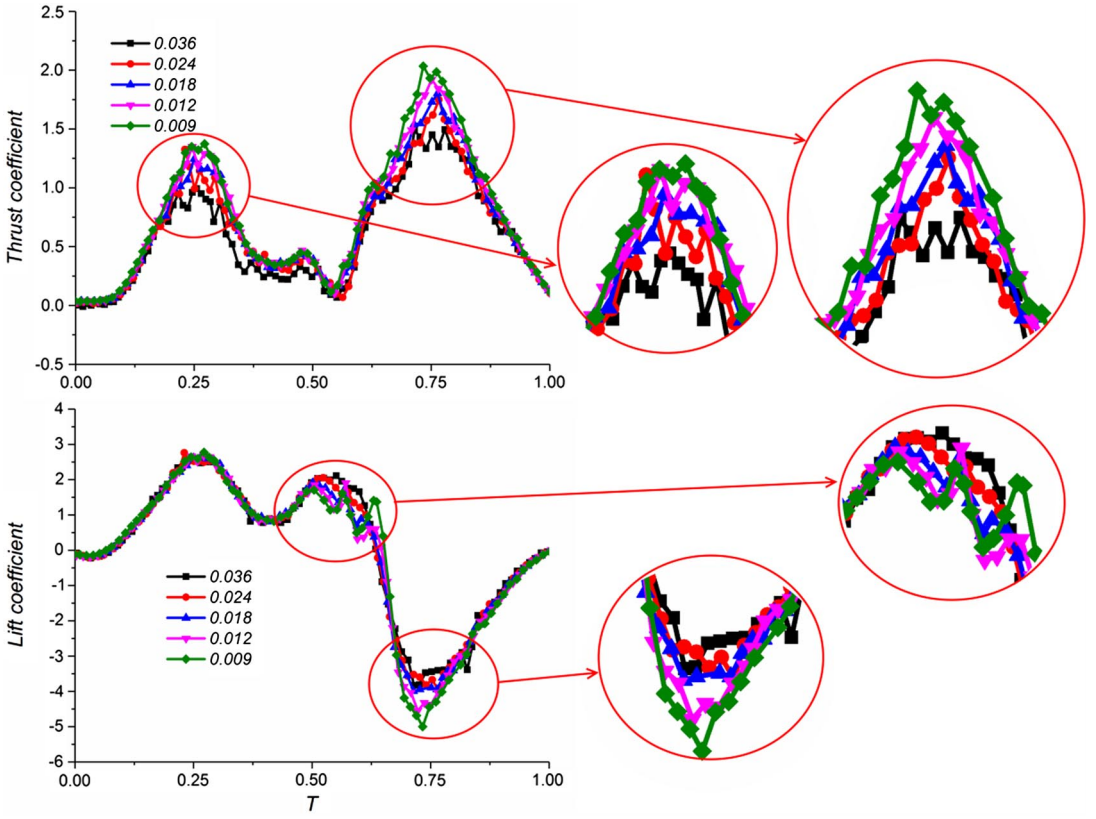


Fig. 7 c_t **and** c_l **results using the kriging skip5 postprocessed wing at minimum grid lengths from 0.009***c* **to 0.036***c* **over one period, with close-ups.**

Downloaded by TU DELFT on October 22, 2020 | http://arc.aiaa.org | DOI: 10.2514/1.J056482

discussed in the earlier experimental setup section (Sec. II). These include accurately capturing and tracking the dots on the fast flapping wings using two to three cameras. Moreover, it is also important to ensure the stability and accuracy of the numerical solver, especially when the wings come in close contact or intersect.

In a previous study by Tay et al. [15], due to the limitation of the solver, it was therefore not possible to fully validate the thrust coefficient. The comparison of the experimental and numerical results at the "clap" portion of the flapping cycle was good, but there was a discrepancy during the "fling" portion. We seek to improve the validation in this study. Besides thrust, we also investigate the drag experienced by the wing. Previous investigators such as Tay et al. [36] and Deng et al. [13] have only focused on the analysis of thrust.

The second objective of this study is to analyze the simulation results through the force and pressure/vorticity contour plots. This will enable us to better understand the underlying aerodynamics of the four-wing flapping-wing MAV.

A. Methodology

A previous study by Tay et al. [15] discussed using the method of kriging interpolation [21–23] to postprocess the raw wing deformation data. The results showed that the kriging postprocessed wing data gave as smoother force variation as compared to that of the raw data. Hence, in the current study, we use the kriging postprocessed wing deformation data (with 17×11 grid points on the wing) for all subsequent simulations. In the original full datasets, there are 100 sampled snapshots of a flapping cycle obtained from the cameras. Ideally, more sampled snapshots should give a more accurate description of the wing deformation. However, due to the wing waviness problem mentioned in the experimental setup section (Sec. II), it is beneficial to skip some data in the time steps. The results by Tay et al. [15] have shown that using 20 time steps (in other words, using one out of five time steps), together with the kriging interpolation, gives good results, and hence it is chosen. A similar methodology has also been employed by Deng et al. [13] in their simulations. We refer to this wing as the kriging skip5 postprocessed wing. More details about the postprocessing of the wing using kriging interpolation is given in Sec. IV.C.

Table 1 RMS error for $dx = 0.012c$ to $0.036c$

Dx	RMS error
$0.036c$	0.23
$0.024c$	0.18
$0.018c$	0.12
$0.012c$	0.07

One restriction of the current IBM solver is that the wing body must have a certain thickness. This is because the IBM is implicitly (but not explicitly) enforced in the Poisson equation in the fractional step. Hence, there is a need for internal points. For this reason, the wing is thickened to obtain a 3% thickness of the chord length by creating a surface on top of and below the original zero-thickness wing body. During simulations, the IBM solver also requires the positions, velocities, and accelerations of particular points on the wing body at a certain time step. They are computed in the numerical solver using fast Fourier transform interpolation.

B. Initial Wing Processing

As mentioned earlier in the experimental setup (Sec. II), only one of the four DelFly wings is captured by the high-speed cameras. We obtain the other three wings through the following steps:

1) The x, y, and z coordinates of the captured wing are analyzed to produce a stereolithography 3-D file. Thickness is also added to the wing in the process.

2) Because the center of rotation is unknown, it is required to approximate the center of rotation of the wing. From the frontal view of the DelFly, a straight line is drawn following the wingspan of the captured wing and extrapolated at three different time instants. These time instants correspond to the two extreme positions of the wings and at the midstroke. The point where the lines meet is the approximate center of rotation.

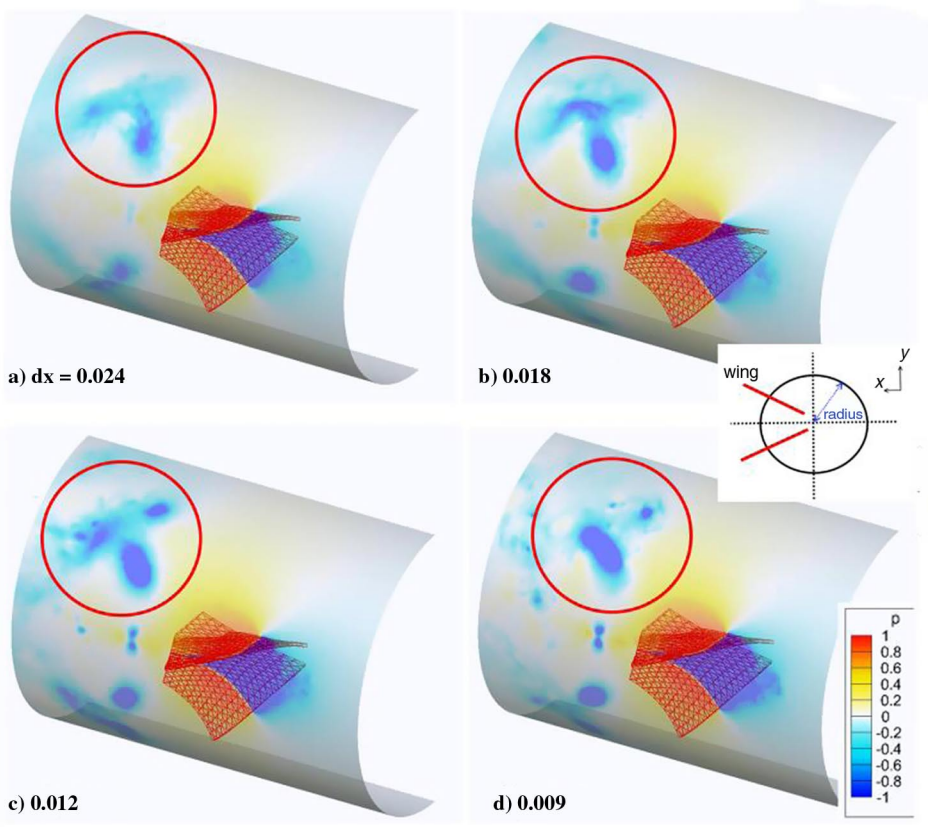


Fig. 8 Pressure contours results at radius of 1.35*c* using the kriging skip5 postprocessed wing at minimum grid lengths of a) 0.024, b) 0.018, c) 0.012, and d) 0.009*c* at a time of 0.64T.

3) The wing is shifted such that the center of rotation coincides with the origin.

4. The wing is rotated by −12 deg (with reference to Fig. 9) to offset the dihedral angle.

5) Denoting the current wing as the upper wing, a mirror plane is used to create the lower wing.

6) The upper and lower wings are shifted up and down along the *y* axis (with reference to Fig. 9), respectively, to ensure a minimum gap of 0.05*c* between the wings.

7) The wing is rotated by 12 deg to obtain back the dihedral angle.

8) The left upper and lower wings are created by reflecting the right upper and lower wings. However, because a symmetry condition is used for the numerical solver, this is not currently required.

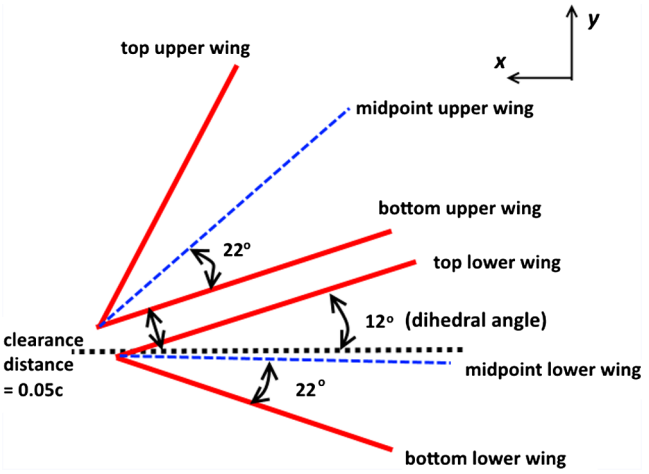


Fig. 9 Geometric flapping parameters of the DelFly's wings from the frontal view.

Figure 10a shows an actual screenshot of the DelFly when the wings' leading edges are at their closest position. In the previous study by Tay et al. [15], this minimum gap occurred during the fling stage when the trailing edges of the two wings were at their closest positions (Fig. 10c). This was to introduce some clearance between the wings to ensure the solver's stability. However, as shown in Fig. 10b, this resulted in a large gap when the wings' leading edges were at their closest position, which was not representative of the actual scenario. In the current study, we ensure a minimum gap of 0.05*c* between the wings' leading edges (Fig. 10d), similar to that of the actual DelFly. In the actual DelFly, the wings touched one another during the fling stage. Due to the errors mentioned earlier, as well as the artificial wing thickness imposed, some brief intersection occurred between the wings during the fling stage (Fig. 10e). Due to improvements in the IBM solver, the simulations could run without divergence.

C. Kriging Interpolations

Kriging regression was developed in the field of geostatistics, as mentioned by Matheron [21], and independently in the field of meteorology, as mentioned by Gandin [22]. An overview of kriging can be found in the work of Cressie [23]. When deriving kriging in a Bayesian framework [37,38], we find that the error covariance matrix can represent individual measurement uncertainties, as mentioned by de Baar et al. [39].

In the present application, the kriging "locations" are the chordwise, spanwise, and timewise coordinates of the dots on the wings, whereas the "data" are the Cartesian coordinates of the dots observed in the experiment. With kriging, we predict the Cartesian coordinates of the wing, depending on the experimental data. We use a Gaussian covariance function, which is modified to ensure periodicity in time. The triangulation distance is used as a proxy for the uncertainties in the position data. The kriging prediction results in an analytical description of the wing surface, which we use to define

Downloaded by TU DELFT on October 22, 2020 | http://arc.aiaa.org | DOI: 10.2514/1.J056482

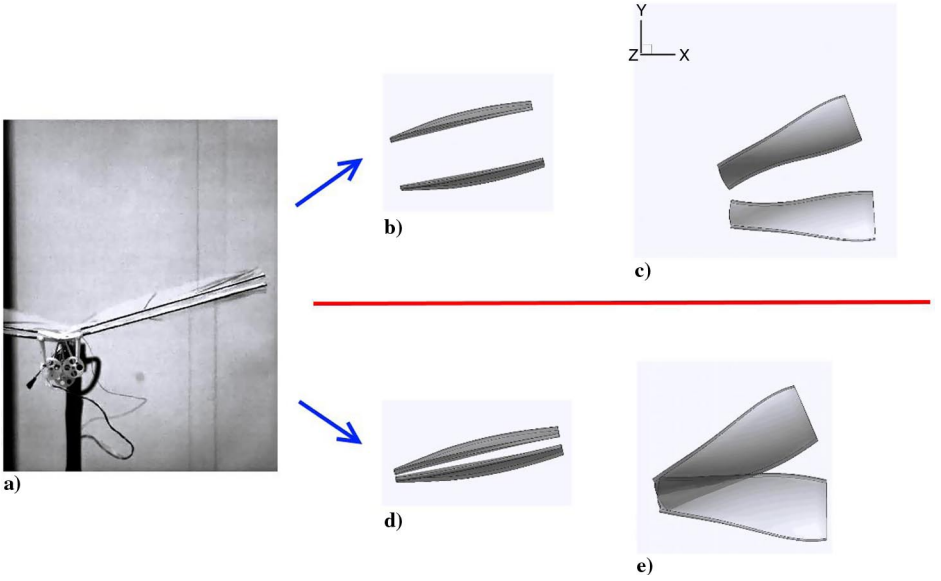
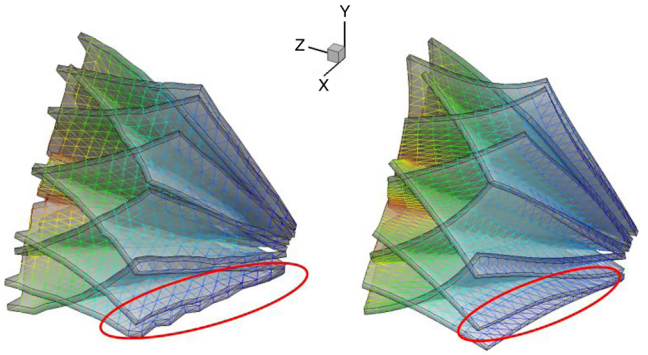


Fig. 10 Actual DelFly wings' screenshot (Fig. 10a), compared to its previous (Figs. 10b and 10c) and current (Figs. 10d and 10e) configurations.

Downloaded by TU DELFT on October 22, 2020 | http://arc.aiaa.org | DOI: 10.2514/1.J056482

the geometry for the computational fluid dynamics (CFD) solver and to obtain the required time derivatives.

A comparison between the raw noninterpolated and kriging interpolated wings is shown in Fig. 11. Only 1/10th of the timeframes is shown for clarity. Ideally, in the actual DelFly wing, the leading edge as shown should be straight because it is attached to the carbon rod. However, the leading edge of final raw digitized wing output is not straight at some instances in time. After kriging interpolation, the leading edge of the digitized wing is smoothened to remove the ragged edges, as indicated by the red circled region in Fig. 11. This shows that there is an improvement due to the use of kriging interpolation. Furthermore, we perform a validation on the accuracy of the kriging regression of the digitized wing's image data. Figure 12 shows the convergence of the kriging prediction error. When we gradually increase the number of training images that are used for the kriging regression, thus decreasing the time between images, we can more accurately predict the remaining data. The accuracy of the kriging prediction is measured by the root-mean-squared (rms) error of the prediction of the remaining data. From Fig. 12, when we decrease the time between training images, the prediction rms error first decreases rapidly. Then, when the rms error reaches the measurement uncertainty of the data (as determined from the triangulation distance), the rms error levels off. The time between images that we presently use results in a prediction rms error that is well below the measurement uncertainty.



a) Raw data **b) Kriging interpolated**

Fig. 11 Comparison of a) raw noninterpolated and b) kriging interpolated wings.

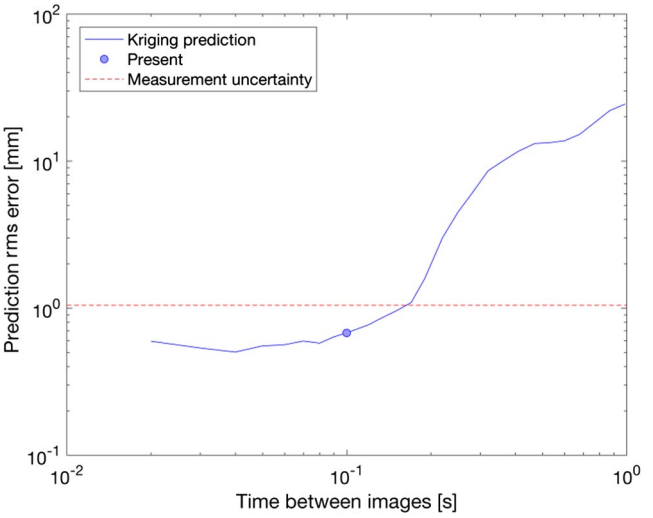


Fig. 12 Graph showing the decrease in the rms error as the time between image decreases.

D. Simulation Parameters

This section discusses the parameters used in the simulations that correspond to the conditions of the wind-tunnel experiments, where the wing deformation and force results are obtained. The DelFly used in the experiment is very similar to the actual flying model under the hovering condition, with the main difference being that the flapping rate of the flying model is higher, at about 13 Hz. Figure 9 shows the geometric parameters of the DelFly's wings. The stroke amplitude of each wing is 22 deg, whereas the dihedral angle is 12 deg. The Reynolds number Re is calculated using the following:

$$Re = \frac{U_{\text{ref}} c}{\upsilon} \tag{7}$$

where U_{ref}, c, and υ are the average wing tip velocity, the chord length, and the kinematic viscosity. The velocity is calculated to be 1.72 m/s, using the flapping frequency and half-wingspan of 0.14 m. With a root chord length of 0.08 m, the Reynolds number Re is 8775. The reduced frequency k is given as follows:

$$k = \frac{fc}{U_{\text{ref}}} \tag{8}$$

Table 2 Parameters of the hovering DelFly

Parameter	Value
Reynolds number Re	8775
Mean wing chord	0.08 m
Average tip velocity	1.72 m/s
Frequency	8 Hz
Reduced frequency k	0.372

where f is the actual flapping frequency. With the actual flapping frequency at 8 Hz, the reduced frequency k is calculated to be 0.372. The parameters of the DelFly are summarized in Table 2.

V. Results and Discussion

The simulations using the kriging postprocessed skip5 wing are performed using the IBM solver. The simulations are performed in quiescent flow for three periods, which are sufficient for the forces to reach an almost periodical stage. The CFD results will be compared with the experimental force results. Furthermore, we will analyze the flow around the wing by means of pressure and vorticity contour plots.

A. Experimental/Numerical Force Results Comparison

First, we concentrate on the experimental data, which have been filtered using different cutoff frequencies. Figure 13 shows the comparison of the experimental thrust coefficient c_t results filtered with cutoff at 2.5, 3.5, 8.5, 9.5, and 10.5 times the flapping frequency over one period. The purpose of filtering is to remove unwanted noise and inertial force, as well as to only represent the true aerodynamic force data. As mentioned earlier in the experimental setup (Sec. II), the vacuum test shows that the cutoff frequency should be 2.5 times. The typical cutoff frequency uses ranges from 2.5 (Nguyen et al. [2] and Percin et al. [17]) to 4 (Deng et al. [40]). As shown in Fig. 13, c_t at 20 and 28 Hz gives very simple graphs with only two peaks. However, the peaks for c_t at 20 Hz are lower than that of 28 Hz. On the other hand, the trough for c_t in region c is higher for the 20 Hz case as compared to the 28 Hz case. Increasing the cutoff frequency to 80 Hz** shows increasing variations in the force graph, as shown by the circled regions. More details of the thrust variation are preserved and, at the same time, the amount of noise filtered out is smaller. Unfortunately, there is no way to differentiate between both of them. Besides the vacuum test, another way to check is through comparison with numerical simulation results.

Figure 14 shows the comparison of experimental c_t filtered at 20, 28, and 68 Hz with the old and new numerical c_t results for the kriging postprocessed skip5 wing over one period. Dotted lines 1, 2, and 3 correspond to times of 1.25T, 1.48T, and 1.72T, respectively. As mentioned earlier, the old/new numerical results use the old/improved solver with the minimum 5% trailing-edge/leading-edge gap, respectively. Comparing between the old and new numerical results, one can observe that they are very similar up to the vertical dotted line (labeled 1), but between 1 and 2, the difference begins to surface, with a minimum hump appearing just before a time of 0.5T for the new numerical result. From lines 2 to 3, the difference in magnitude is obvious and, at line 3, there is a large difference in the peak value. Dotted lines 1, 2, and 3 correspond to approximately the middle of the clap, the transition from the clap to the fling, and the middle of the fling phase, respectively. In the old simulations, the gap between the upper and lower wings was shifted such that, although the minimum gap was 5% of the chord at the trailing edges, their gap became rather large during the fling phase. This was not representative of the actual scenario. On the other hand, a minimum gap of 5% chord between the leading edges of the new wings is a closer representation. Interestingly, despite the difference in the gap between the new and old wings, there is no difference in c_t during the clap phase.

**The results between the cutoff frequencies of 28 and 68 Hz are not shown because they do not show much variation.

Comparing between the current IBM c_t with the experimental one at 20 Hz, we observe that both their first peak values match very well, whereas the second peak value of the IBM c_t is 13% smaller than that of 20 Hz. However, the width of the parabola of the numerical result's graph tends to be smaller than that of the experimental result, with the difference being more obvious in the region between times of 0.25T–0.5T and 0.75T–1T. Comparing between the current IBM c_t with the experimental one at 28 and 68 Hz, we observe that the peaks of the numerical result are still slightly lower than that of the experiment. As shown in Fig. 14, the peak value differences between IBM skip5 and c_t from the 28 Hz results are approximately 13% for both the low and high peaks. However, both numerical and experimental results have the same ratio between the lower and taller peaks (∼1.3). On the other hand, the peak value differences between IBM skip5 and c_t from the 68 Hz results are approximately 13 and 24% for the low and high peaks, respectively. Past experiments by Groen et al. [5] and Tenaglia et al. [41] have also shown that the fling phase produces higher thrust as compared to the clap phase.

The main difference between the 28 and 68 Hz experimental data occurs at dotted line 2, which corresponds to the transition from the clap to the fling instant. In this region, the 68 Hz experimental data correlate better with the current numerical result. In general, in comparison with all the different cutoff frequencies, the overall shape and relative force peak heights are similar and compare reasonably well with the numerical result. Both the experiments and simulations inherently have their own errors; hence, it does not mean that either the experimental or numerical results are completely correct. In view of all this evidence, which includes the current experimental data at different cutoff frequencies and the numerical result, we can predict with confidence that a reasonable cutoff frequency should be between 28 and 68 Hz. However, we are not able to conclusively state what the exact cutoff frequency should be. Nevertheless, there is overall good correspondence between the experimental and numerical data.

B. Flowfield Analysis

Figure 15 shows the Q criterion (formulated by Hunt et al. [42]) is a 100 isosurface superimposed with the pressure contour from the numerical simulation over one period. Times of 0.25T, 0.48T, and 0.72T correspond to dotted lines 1, 2, and 3 in Fig. 14. (Parts of the figures have been grayscaled to reduce distraction. The diagrams are to be read in a circular sequence because they show periodic motion.) One of the wings is shown in the wire frame to reveal what is happening in the clap–fling region. Starting from the clapping phase (Fig. 15a), the leading-edge vortex (LEV), tip vortex (TV), and trailing-edge vortex (TEV) start to build up, with high pressure on the pressure side of the wing. By a time of 0.25T, the LEV, TV and LEV (circled red) are well formed, giving the first force peak in Fig. 14 (dotted line 1) and remains stable until near the wing rotation instant (Fig. 15c). The TEV breaks up first, followed by the LEV and TV as the wings touch one another briefly. The fling phase starts as the wings peel open and at a time of 0.72T, we can observe the very low pressure between the wings (circled red in Fig. 15d). The LEV and TV have formed and this gives the higher second force peak. Up until a time of 0.92T (Fig. 15e), they remain stable. They break up once again at the end of the fling/starting of the clap phase (Fig. 15f).

Due to the relatively high Re, there is a larger range of length scales and as a result, some important features may be obscure by the dense vortical structures in Fig. 15. Hence, we use instantaneous streamlines in Fig. 16 to give an alternative view. At a time of 0.12T, which is the transition between end of fling and start of clap, we observe the formation of the "V-shaped linked" vortex (circled red), which is subsequently shed. It is also observed in Fig. 15a. The formation starts at a time of 0.84T (or −0.16 T) as the wings separates and forms a vortex link between them. The link grows in strength to form the V-shaped vortical structure, as shown in both Figs. 15a and 16a.

At a time of 0.72T, when the wings start to peel apart, we observe the strong influx of air due to the suction effect. This is evident from the streamlines between the wings, as shown in Fig. 16c. As mentioned earlier, the LEV and TV start to grow (circled red), as seen

Downloaded by TU DELFT on October 22, 2020 | http://arc.aiaa.org | DOI: 10.2514/1.J056482

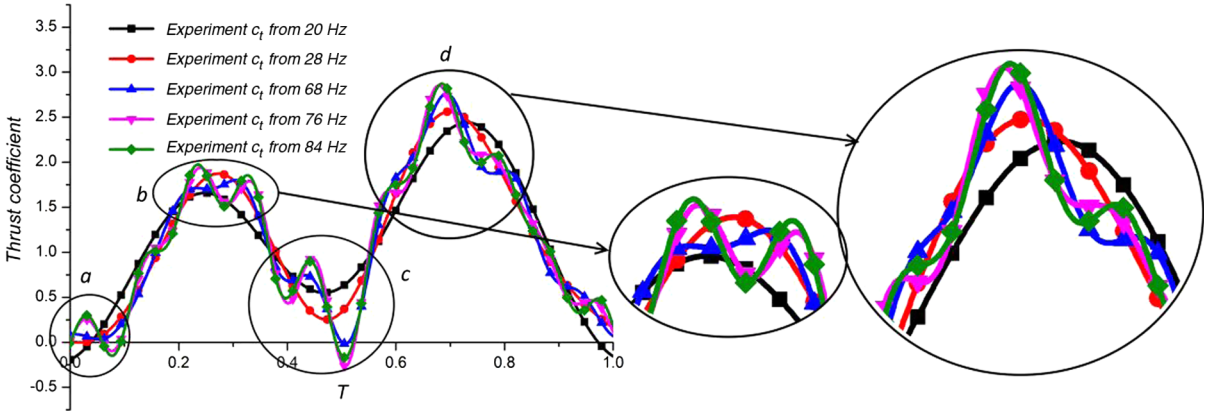


Fig. 13 Comparison of experimental thrust coefficient c_t results filtered with cutoff at 2.5, 3.5, 8.5, 9.5, and 10.5 times the flapping frequency over one period. Circles *a* to *d* refer to areas of interest.

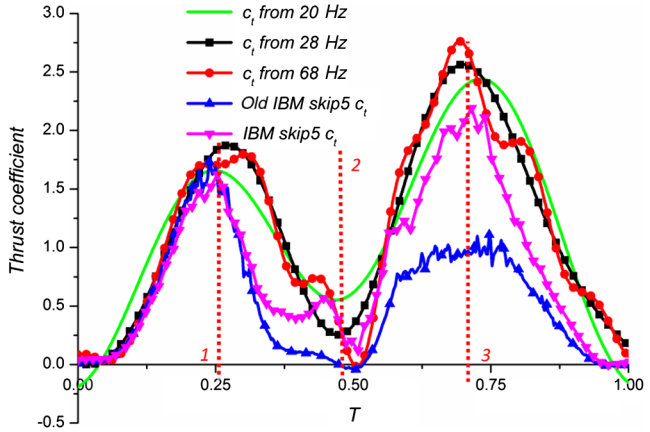


Fig. 14 Comparison of the experimental and numerical thrust coefficient c_t results for the Kriging post-processed skip5 wing over one flapping period T.

at the times of 0.84T and 0.96T in Fig. 16. However, the TEV is almost nonexistent due to the close proximity of the wings' trailing edges. This creates a vortical asymmetry, enhances circulation, and increases lift [6,43–45].

With regard to the V-shaped linked vortex, similar vortical structures, differing in shape and timing, have been observed in 3-D clap and fling simulations [43,46] and DelFly PIV experiments [41,47,48]. As mentioned in the work of Zhang [43], the vortex link provides a strong downwash that helps to further enhance the thrust. In a previous PIV experiment involving the DelFly in forward flight, as described by Percin et al. [19], a similar "U-shaped" vortical structure is also observed but at a slightly later time of 0.31T. Similarly, Tenaglia et al. [41], who performed PIV experiments with DelFly in hovering conditions but at a higher flapping frequency of 11.2 Hz, also mentioned a similar TEV tube being observed. One reason for the difference in shape and timing may be because the DelFly was in a forward-flight condition, as described by Percin et al. [19]. The difference in shape and timing between the current V-shaped linked vortex and the other vortical structures was most likely due to the different wing kinematics and fight conditions involved. Lastly, the vortex is only observable from a radius of around $1.35c$ from the wing rotation center, as shown in Fig. 17.

C. Drag Analysis

Besides considering the thrust in the earlier portion of the section, we also consider the drag c_d experienced by the wings as they clap and fling. The drag experienced by the wings as they flap has not been considered by earlier studies because the focus has always been on the thrust generated. Previous studies on thrust by Tay et al. [36] and Deng et al. [13] showed that the clap and fling configuration generated a higher thrust as compared to a single-wing configuration. As for drag, earlier clap and fling studies by Miller and Peskin [45,49] showed that clap and fling motions in insects at very low Reynolds numbers *Re* (∼8 to 128) could generate drag forces up to 10 times more than motions without wing–wing interaction. However, flexibility in the wings could reduce the maximum drag force by about 50%. Hence, it is interesting to investigate the difference in the drag magnitude between the clap and fling and the single-wing configurations for this FMAV.

Figure 18 shows the schematic diagram of the wings experiencing drag as they flap. (Red and blue lines indicate the two left wings. The green arrow indicates the flapping direction of the two wings at that instant.) The drag force is perpendicular to the wing and opposite to the direction of the flapping motion. Hence, it is not the negative value of the thrust mentioned earlier. Here, we are referring to the opposition force the wing faces as it flaps. We focus our analysis on the upper wing (as shown in Fig. 9) because that of the lower wing should be similar. However, there will be some differences in the magnitude and variation of the drag over one cycle due to the dihedral angle of 12 deg, as shown in Fig. 9. Due to the high deformation of the membrane wing, it is difficult to get the exact drag force acting perpendicular to the wing. Instead, we define our drag force to be perpendicular to the leading edge of the wing and in the xy plane to simplify the calculation. This allows us to obtain an estimate of the drag force acting on the wing. To obtain the drag force coefficient, we resolve the forces in the x and y directions (c_x and c_y) along the direction perpendicular to the leading edge of the wing. Ideally, the drag force will reverse its direction after half a cycle as the wing reverses its flapping motion. However, in the case of the DelFly, we observe that, due to the wing's deformation, although the leading edge has started to reverse its flapping direction after half a cycle, the portion of wing from the midchord to the trailing edge still has not reversed its direction. In other words, it is still in the clap phase, although the leading edge has started its fling phase. However, because different portions of the wing reverse their directions at different instants due to the irregular deformation, we reverse the drag force direction in our calculation at a time of 0.5T for simplification. Hence, at around a time of 0.5T, negative drag can be observed.

From time = 0 to 0.5T,

$$c_d = c_y \cos(\theta) - c_x \sin(\theta) \tag{9}$$

From $t > 0.5$T to T

$$c_d = -[c_y \cos(\theta) - c_x \sin(\theta)] \tag{10}$$

where θ is the angle that the leading edge of the wing makes with the positive y axis.

For this drag comparison, a new simulation using a single (upper wing) wing is performed. However, it has to be noted that the wing deformation used is based on the DelFly, which has two pairs of wings. Hence, especially near the instants where the two wings clap,

Downloaded by TU DELFT on October 22, 2020 | http://arc.aiaa.org | DOI: 10.2514/1.J056482

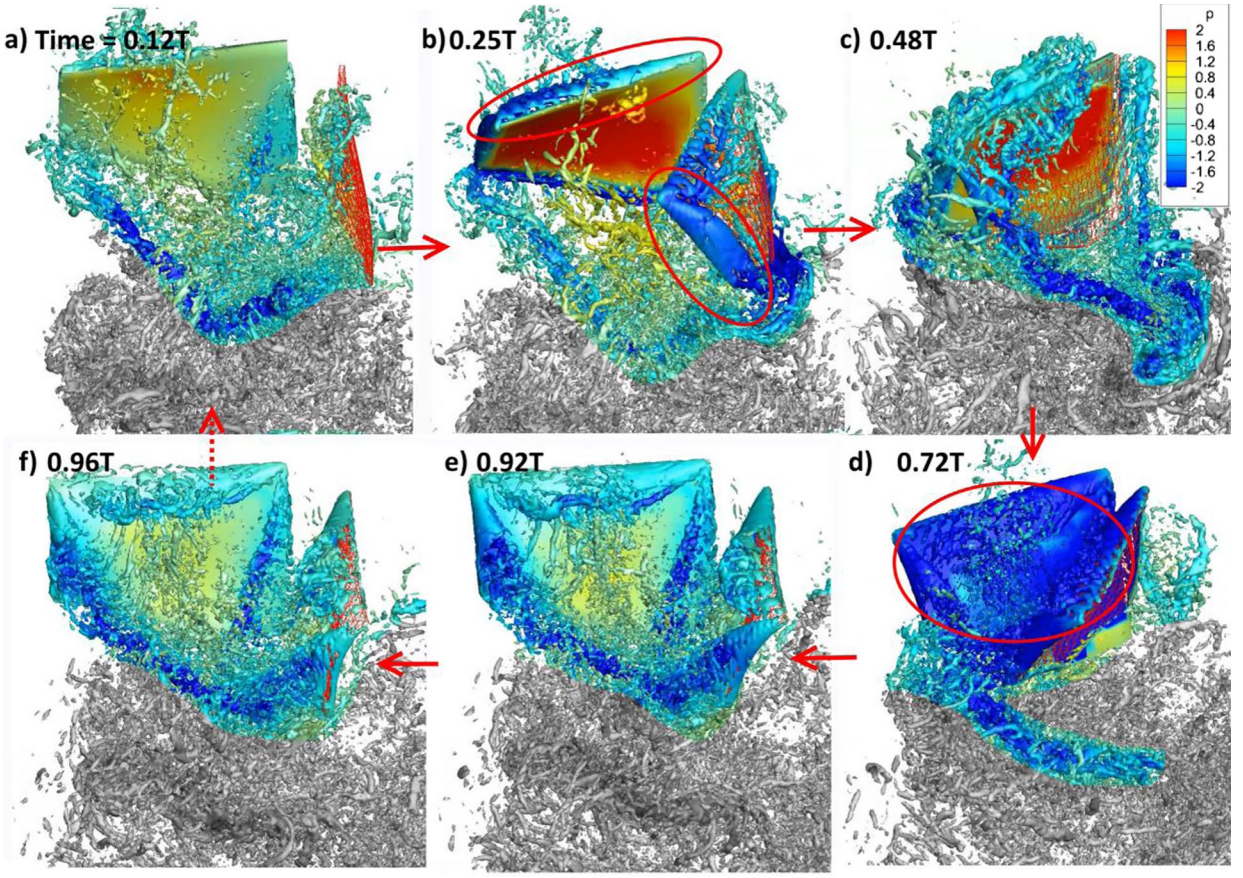


Fig. 15 Isosurface plotted at Q criterion of 100 superimposed with pressure contour from numerical simulation over one period.

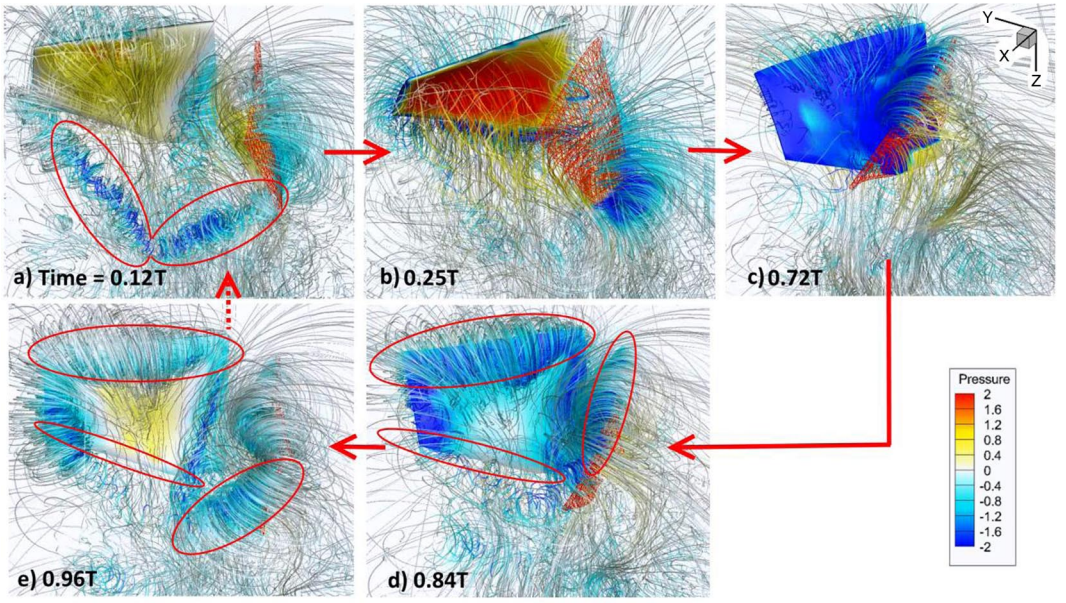
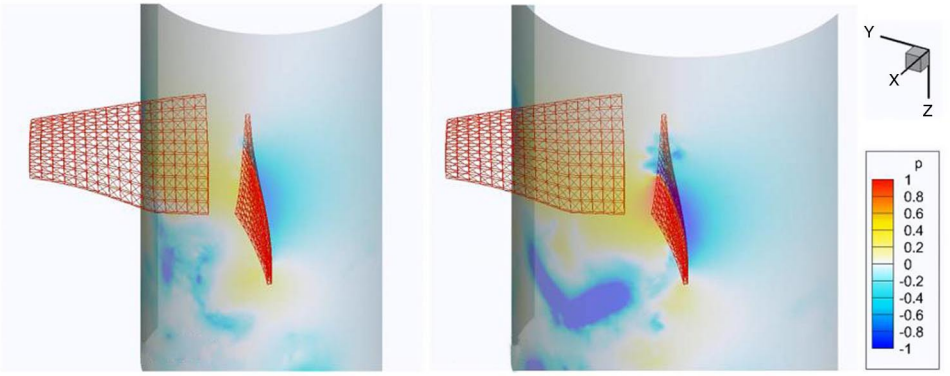


Fig. 16 Instantaneous streamlines superimposed with pressure contour at different instants in time. Diagrams are to be read in a circular sequence because they show periodic motion.

the wing deformation will be different from that of an actual single-wing configuration. As the wings fling and move apart from one another, the difference will be less. Nevertheless, in this comparison, we should be able to obtain an estimate of the difference in drag magnitude between the clap and fling and the single-wing configurations. Figure 19 shows the variation of θ, c_t, and c_d (DelFly, single) over one period. At the start, the red wing (upper wing) is in an almost vertical orientation and θ increases from 0 deg. We can observe from the graph that, similar to the thrust coefficient, the drag coefficient has two peaks, with the fling's peak having a higher magnitude as compared to the flap's peak. This is because it takes more effort to overcome the vacuum between the upper and lower wings during fling as compared to the flap. Moreover, similar to the thrust force, the drag force is almost the same during the clap phase: in both the clap and fling and single-wing configurations. During the fling phase, the magnitude of c_d of the clap and fling configuration is about 2.5 times that of the single-wing configuration. This ratio is similar to that of the thrust. Hence, the difference is not as large as

Downloaded by TU DELFT on October 22, 2020 | http://arc.aiaa.org | DOI: 10.2514/1.J056482



a) Radius = 1.00 *c* b) 1.35 *c*

Fig. 17 Pressure contours at radii of a) 1.00*c* and b) 1.35*c*.

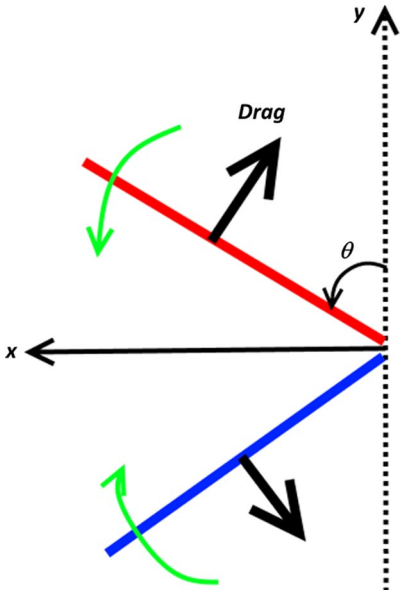


Fig. 18 Schematic diagram showing wings experiencing drag as they flap. Drag forces (black arrows) on the wings are always perpendicular and opposite in direction to the motion of the wings.

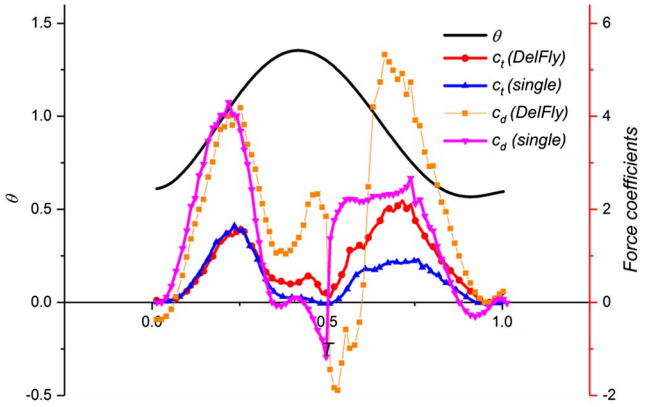


Fig. 19 Graphs showing the variations of θ, c_t, and c_d (DelFly, single) over one period.

those low-Reynolds-number cases mentioned by Miller and Peskin [45,49]. This is mainly due to the high Reynolds number Re as well as the high flexibility of the wing in the current case. This investigation shows that the clap and fling configuration is still a viable FMAV design, especially when higher thrust is required.

D. Future Work

The simulation force results compare well with the experiment. With the success in using the wing deformation data to run the simulations, it opens up opportunities for FMAV design-related problems. It will be possible to investigate the possible impact of changes in the configuration or flight conditions. These simulations can be classified into two categories: one where the wing deformation will only be slightly affected by additional modifications to the original standard configuration, and another where the wing deformation will change due to parameters to be investigated. In that case, it will not be possible to reuse the current wing deformation data. Initial studies can first be performed to assess if it is necessary to repeat wing deformation capture for each set of parameters. Two to three wing deformation captures should be sufficient to confirm if it is necessary.

An example of the first scenario is a control surfaces analysis. In most FMAVs, control surfaces such as the tail rudder are still used due to their simplicity and effectiveness. However, it is difficult to assess their effects with respect to different sizes and shapes. By adding control surfaces in the simulation, we can obtain a better understanding of their effects. The use of actual wing deformation data increases the realism of the simulation, as compared to using a prescribed simplified sinusoidal pitching and flapping motion. Moreover, performing a full FSI simulation together with the control surface analysis will further increase the already high computational resources. The control surfaces of FMAVs [1,2] are usually more than one chord length from the wings' trailing edges. Hence, we can assume that the wings' deformation will only be slightly affected by change in control surface variations.

In the second scenario, the wing deformation changes due to the parameters to be investigated. In this case, the wing deformation measurements have to be repeated for each set of data. To speed up this process, we can reduce the number of markers (in opposition to the original 166 blue dots) on the wings. Another alternative is to improve the automation of the marker detection process. For example, initial testing of the latest version of Hedrick's MATLAB tool for digitizing package [50] has shown that it is possible to track most of the markers over an entire flapping cycle automatically. These improvements greatly speed up the marker point extraction process, allowing us to complete the digitization of the wing over one flapping cycle quickly and efficiently. Some application examples include the following:

1. *Wing Gust Analysis*

The wing gust effect has been studied by Lian [51] and Jones and Yamaleev [52], but they were restricted to either two-dimensional or 3-D prescribed motion, which is very different from a FMAV with membrane wings. Hence, these wing deformation data offer a chance to perform simulations with realistically deforming wings.

2. *Optimization Analysis*

Optimization of the wing through the investigation of the wing shape, thickness, and material can be performed and assessed. With the new wing constructed, simulations can be performed to obtain insights into the new flowfield and force data.

Downloaded by TU DELFT on October 22, 2020 | http://arc.aiaa.org | DOI: 10.2514/1.J056482

VI. Conclusions

Three-dimensional simulations of a biplane flapping membrane wing micro aerial vehicle (MAV) are performed using the wing kinematics captured through stereovision triangulation. Kriging interpolation is used to postprocess the raw deformation data to smoothen the ragged edges of the wings. Furthermore, improvements to the immersed boundary method solver enable us to run simulations with wing intersection. The results show that there is a reasonable agreement between the numerical and experimental data, with the first and second force peaks well captured by the simulations. The flowfield analysis reveals complex vortex formation and shedding. A V-shaped linked vortex is observed, which is similar to the other vortical structures found in 3-D clap and fling simulations [43,46] and DelFly particle image velocimetry (PIV) experiments [41,47]. Results from the wing drag analysis also show that the drag magnitude of the clap and fling configuration is about 2.5 times that of the single-wing configuration. Through the simulations, the flowfields can be visualized through pressure contours and vortical isosurfaces, which allow understanding of their underlying aerodynamics. This may not be possible or is difficult through PIV experiments, especially in the wing vicinity due to laser reflection, as described by Groen et al. [5]. The ability to accurately simulate the flapping MAV with membrane wings also opens up opportunities for FMAV design-related problems. These include the control surfaces, wing gust, and optimization analysis.

Acknowledgments

The computational work for this paper was done with the resources of the National Supercomputing Computer, Singapore. The authors wish to thank the National Supercomputing Computer for their kind support. The digitalized wing deformation kinematics data of the fruit bat have been kindly provided by D. K. Tafti of the Virginia Polytechnic Institute and State University. The authors wish to thank him for his assistance.

References

[1] de Croon, G. C. H. E., Perçin, M., Remes, B. D. W., Ruijsink, R., and de Wagter, C., *The DelFly: Design, Aerodynamics, and Artificial Intelligence of a Flapping Wing Robot*, Springer, Dordrecht, The Netherlands, 2016. doi:10.1007/978-94-017-9208-0

[2] Nguyen, Q. V., Chan, W. L., and Debiasi, M., "Hybrid Design and Performance Tests of a Hovering Insect-Inspired Flapping-Wing Micro Aerial Vehicle," *Journal of Bionic Engineering*, Vol. 13, No. 2, 2016, pp. 235–248. doi:10.1016/S1672-6529(16)60297-4

[3] Keennon, M., Klingebiel, K., Won, H., and Andriukov, A., "Tailless Flapping Wing Propulsion and Control Development for the Nano Hummingbird Micro Air Vehicle," *Proceedings of 68th American Helicopter Society Future Vertical Lift Aircraft Design Conference*, San Francisco, Jan. 2012, pp. 1–24.

[4] Percin, M., and van Oudheusden, B. W., "Three-Dimensional Flow Structures and Unsteady Forces on Pitching and Surging Revolving Flat Plates," *Experiments in Fluids*, Vol. 56, No. 2, 2015, pp. 1–19. doi:10.1007/s00348-015-1915-9

[5] Groen, M., Bruggeman, B., Remes, B., Ruijsink, R., van Oudheusden, B. W., and Bijl, H., "Improving Flight Performance of the Flapping Wing MAV DelFly II," *International Micro Air Vehicle Conference and Competitions*, Braunschweig, Germany, 2010, pp. 1–17.

[6] Weis-Fogh, T., "Quick Estimates of Flight Fitness in Hovering Animals, Including Novel Mechanisms for Lift Production," *Journal of Experimental Biology*, Vol. 59, 1973, pp. 169–230.

[7] Garmann, D. J., Visbal, M. R., and Orkwis, P. D., "Three-Dimensional Flow Structure and Aerodynamic Loading on a Low Aspect Ratio, Revolving Wing," *42nd AIAA Fluid Dynamics Conference and Exhibit*, AIAA Paper 2012-3277, 2012, pp. 1–22.

[8] Tian, F.-B., Dai, H., Luo, H., Doyle, J. F., and Rousseau, B., "Fluid–Structure Interaction Involving Large Deformations: 3-D Simulations and Applications to Biological Systems," *Journal of Computational Physics*, Vol. 258, Feb. 2014, pp. 451–469. doi:10.1016/j.jcp.2013.10.047

[9] Nakata, T., and Liu, H., "A Fluid–Structure Interaction Model of Insect Flight with Flexible Wings," *Journal of Computational Physics*, Vol. 231, Feb. 2012, pp. 1822–1847. doi:10.1016/j.jcp.2011.11.005

[10] Viswanath, K., Nagendra, K., and Tafti, D. K., "Climbing Flight of a Fruit Bat Deconstructed," *52nd Aerospace Sciences Meeting*, AIAA Paper 2014-0220, 2014, pp. 1–24.

[11] Riskin, D. K., Willis, D. J., Iriarte-Díaz, J., Hedrick, T. L., Kostandov, M., Chen, J., Laidlaw, D. H., Breuer, K. S., and Swartz, S. M., "Quantifying the Complexity of Bat Wing Kinematics," *Journal of Theoretical Biology*, Vol. 254, No. 3, 2008, pp. 604–615. doi:10.1016/j.jtbi.2008.06.011

[12] Nakata, T., Liu, H., Tanaka, Y., Nishihashi, N., Wang, X., and Sato, A., "Aerodynamics of a Bio-Inspired Flexible Flapping-Wing Micro Air Vehicle," *Bioinspiration and Biomimetics*, Vol. 6, Dec. 2011, Paper 45002. doi:10.1088/1748-3182/6/4/045002

[13] Deng, S., Percin, M., van Oudheusden, B. W., Bijl, H., Remes, B., and Xiao, T., "Numerical Simulation of a Flexible X-Wing Flapping-Wing Micro Air Vehicle," *AIAA Journal*, Vol. 55, No. 7, 2017, pp. 2295–2306. doi:10.2514/1.J054816

[14] Mittal, R., and Iaccarino, G., "Immersed Boundary Methods," *Annual Review of Fluid Mechanics*, Vol. 37, Jan. 2005, pp. 239–261. doi:10.1146/annurev.fluid.37.061903.175743

[15] Tay, W. B., de Baar, J. H. S., Percin, M., Deng, S., and van Oudheusden, B. W., "Numerical Simulation of a Flapping Wing MAV Based on Wing Deformation Capture Analysis," *34th AIAA Applied Aerodynamics Conference*, AIAA Paper 2016-3552, 2016, pp. 1–13.

[16] Lighthill, M. J., "On the Weis-Fogh Mechanism of Lift Generation," *Journal of Fluid Mechanics*, Vol. 60, No. 1, 1973, pp. 1–17. doi:10.1017/S0022112073000017

[17] Percin, M., van Oudheusden, B. W., de Croon, G. C. H. E., and Remes, B., "Force Generation and Wing Deformation Characteristics of a Flapping-Wing Micro Air Vehicle 'DelFly II' in Hovering Flight," *Bioinspiration and Biomimetics*, Vol. 11, May 2016, Paper 036014. doi:10.1088/1748-3190/11/3/036014

[18] de Clercq, K. M. E., de Kat, R., Remes, B., van Oudheusden, B. W., and Bijl, H., "Aerodynamic Experiments on Delfly II : Unsteady Lift Enhancement," *International Journal of Micro Air Vehicles*, Vol. 1, No. 4, 2009, pp. 255–262. doi:10.1260/175682909790291465

[19] de Clercq, K. M. E., "Flow Visualization and Force Measurements on a Hovering Flapping-Wing MAV 'DelFly II'," Delft Univ. of Technology, Delft, The Netherlands, 2009.

[20] Percin, M., van Oudheusden, B. W., Eisma, H. E., and Remes, B. D. W., "Three-Dimensional Vortex Wake Structure of a Flapping-Wing Micro Aerial Vehicle in Forward Flight Configuration," *Experiments in Fluids*, Vol. 55, No. 9, 2014, pp. 1806–1821. doi:10.1007/s00348-014-1806-5

[21] Matheron, G., "Principles of Geostatistics," *Economic Geology*, Vol. 58, Dec. 1963, pp. 1246–1266. doi:10.2113/gsecongeo.58.8.1246

[22] Gandin, L. S., *Objective Analysis of Meteorological Fields*, Israel Program for Scientific Translation, Leningrad, Russia, 1965, p. 242.

[23] Cressie, N., *Statistics for Spatial Data*, Rev. ed., Wiley, New Jersey, 1993, p. 90.

[24] Yang, J., and Balaras, E., "An Embedded-Boundary Formulation for Large-Eddy Simulation of Turbulent Flows Interacting with Moving Boundaries," *Journal of Computational Physics*, Vol. 215, June 2006, pp. 12–40. doi:10.1016/j.jcp.2005.10.035

[25] Kim, J., Kim, D., and Choi, H., "An Immersed-Boundary Finite-Volume Method for Simulations of Flow In Complex Geometries," *Journal of Computational Physics*, Vol. 171, July 2001, pp. 132–150. doi:10.1006/jcph.2001.6778

[26] Liao, C.-C., Chang, Y.-W., Lin, C.-A., and McDonough, J. M., "Simulating Flows with Moving Rigid Boundary Using Immersed-Boundary Method," *Computers and Fluids*, Vol. 39, Jan. 2010, pp. 152–167. doi:10.1016/j.compfluid.2009.07.011

[27] Kim, D., and Choi, H., "A Second-Order Time-Accurate Finite Volume Method for Unsteady Incompressible Flow on Hybrid Unstructured Grids," *Journal of Computational Physics*, Vol. 162, Aug. 2000, pp. 411–428. doi:10.1006/jcph.2000.6546

[28] Balay, S., Gropp, W. D., McInnes, L. C., and Smith, B. F., "Efficient Management of Parallelism in Object Oriented Numerical Software Libraries," *Modern Software Tools in Scientific Computing*, edited by E. Arge, A. M. Bruaset, and H. P. Langtangen, Birkhauser Boston Inc., Cambridge, MA, 1997, pp. 163–202.

Downloaded by TU DELFT on October 22, 2020 | http://arc.aiaa.org | DOI: 10.2514/1.J056482

[29] Falgout, R. D., Jones, J. E., and Yang, U. M., "The Design and Implementation of Hypre, a Library of Parallel High Performance Preconditioners," *Numerical Solution of Partial Differential Equations on Parallel Computers*, edited by A. M. Bruaset, and A. Tveito, Springer-Verlag, New York, 2006, pp. 267–294.

[30] Shepard, D., "A Two-Dimensional Interpolation Function for Irregularly-Spaced Data," *Proceedings of ACM National Conferenc*, New York, Aug. 1968, pp. 517–524. doi:10.1145/800186.810616

[31] Lee, J., Kim, J., Choi, H., and Yang, K.-S., "Sources of Spurious Force Oscillations from an Immersed Boundary Method for Moving-Body Problems," *Journal of Computational Physics*, Vol. 230, April 2011, pp. 2677–2695. doi:10.1016/j.jcp.2011.01.004

[32] Calderon, D. E., Wang, Z., and Gursul, I., "Lift Enhancement of a Rectangular Wing Undergoing a Small Amplitude Plunging Motion," *48th AIAA Aerospace Sciences Meeting*, AIAA Paper 2010-0386, 2010, pp. 1–18.

[33] Lua, K. B., Lim, T. T., and Yeo, K. S., "Scaling of Aerodynamic Forces of Three-Dimensional Flapping Wings," *AIAA Journal*, Vol. 52, Jan. 2014, pp. 1095–1101. doi:10.2514/1.J052730

[34] Viswanath, K., Nagendra, K., Cotter, J., Frauenthal, M., and Tafti, D. K., "Straight-Line Climbing Flight Aerodynamics of a Fruit Bat," *Physics of Fluids*, Vol. 26, No. 2, 2014, Paper 021901. doi:10.1063/1.4864297

[35] Tay, W. B., Deng, S., van Oudheusden, B. W., and Bijl, H., "Validation of Immersed Boundary Method for the Numerical Simulation of Flapping Wing Flight," *Computers and Fluids*, Vol. 115, July 2015, pp. 226–242. doi:10.1016/j.compfluid.2015.04.009

[36] Tay, W. B., van Oudheusden, B. W., and Bijl, H., "Numerical Simulation of a Flapping Four-Wing Micro-Aerial Vehicle," *Journal of Fluids and Structures*, Vol. 55, May 2015, pp. 237–261. doi:10.1016/j.jfluidstructs.2015.03.003

[37] Wikle, C. K., and Berliner, L. M., "A Bayesian Tutorial for Data Assimilation," *Physica D: Nonlinear Phenomena*, Vol. 230, June 2007, pp. 1–16. doi:10.1016/j.physd.2006.09.017

[38] de Baar, J. H. S., Dwight, R. P., and Bijl, H., "Improvements to Gradient-Enhanced Kriging Using a Bayesian Interpretation," *International Journal for Uncertainty Quantification*, Vol. 4, No. 3, 2014, pp. 205–223. doi:10.1615/Int.J.UncertaintyQuantification.v4.i3

[39] de Baar, J. H. S., Percin, M., Dwight, R. P., van Oudheusden, B. W., and Bijl, H., "Kriging Regression of PIV Data Using a Local Error Estimate," *Experiments in Fluids*, Vol. 55, Jan. 2014, Paper 1650. doi:10.1007/s00348-013-1650-z

[40] Deng, S., Percin, M., van Oudheusden, B. W., Remes, B. D. W., and Bijl, H., "Experimental Investigation on the Aerodynamics of a Bio- Inspired Flexible Flapping Wing Micro Air Vehicle," *International Journal of Micro Air Vehicles*, Vol. 6, No. 2, June 2014, pp. 105–115.

[41] Tenaglia, A., Percin, M., van Oudheusden, B. W., Deng, S., and Remes, B., "Vortex Formation and Force Generation Mechanisms of the DelFly II in Hovering Flight," *Proceedings of International Micro Air Vehicle Conference and Competitions*, Delft, The Netherlands, Aug. 2014, pp. 204–211.

[42] Hunt, J. C. R., Wray, A. A., and Moin, P., "Eddies, Streams, and Convergence Zones in Turbulent Flows," *Proceedings of the Center for turbulence research Summer Program*, Santa Clara County, 1988, pp. 193–208.

[43] Zhang, L., "Unsteady Aerodynamics of Flapping Wings," Ph.D. Dissertation, National Univ. of Singapore, Singapore, 2013.

[44] Tay, W. B., "Effect of Different Types of Wing-Wing Interactions in Flapping MAVs," *Journal of Bionic Engineering*, Vol. 14, No. 1, 2017, pp. 60–74. doi:10.1016/S1672-6529(16)60378-5

[45] Miller, L. A., and Peskin, C. S., "A Computational Fluid Dynamics of 'Clap and Fling' in the Smallest Insects," *Journal of Experimental Biology*, Vol. 208, Jan. 2005, pp. 195–212. doi:10.1242/jeb.01376

[46] Kolomenskiy, D., Moffatt, H. K., Farge, M., and Schneider, K., "Two- and Three-Dimensional Numerical Simulations of the Clap–Fling–Sweep of Hovering Insects," *Journal of Fluids and Structures*, Vol. 27, July 2011, pp. 784–791. doi:10.1016/j.jfluidstructs.2011.05.002

[47] Percin, M., Eisma, H. E., van Oudheusden, B. W., Remes, B., Ruijsink, R., and de Wagter, C., "Flow Visualization in the Wake of Flapping-Wing MAV 'DelFly II' in Forward Flight," *30th AIAA Applied Aerodynamics Conference*, AIAA Paper 2012-2664, 2012, pp. 1–12.

[48] Percin, M., van Oudheusden, B. W., and Remes, B., "Flow Structures Around a Flapping-Wing Micro Air Vehicle Performing a Clap-and-Peel Motion," *AIAA Journal*, Vol. 55, No. 4, 2017, pp. 1251–1264. doi:10.2514/1.J055146

[49] Miller, L. A., and Peskin, C. S., "Flexible Clap and Fling in Tiny Insect Flight," *Journal of Experimental Biology*, Vol. 212, Oct. 2009, pp. 3076–3090. doi:10.1242/jeb.028662

[50] Hedrick, T. L., "Software Techniques for Two- and Three-Dimensional Kinematic Measurements of Biological and Biomimetic Systems," *Bioinspiration and Biomimetics*, Vol. 3, July 2008, Paper 34001. doi:10.1088/1748-3182/3/3/034001

[51] Lian, Y., "Numerical Study of a Flapping Airfoil in Gusty Environments," *27th AIAA Applied Aerodynamics Conference*, AIAA Paper 2009-3952, 2009, pp. 1–13.

[52] Jones, M., and Yamaleev, N. K., "The Effect of a Gust on the Flapping Wing Performance," *50th AIAA Aerospace Sciences Meeting*, AIAA Paper 2012-1080, 2012, pp. 1–9.

M. J. Patil
Associate Editor

Downloaded by TU DELFT on October 22, 2020 | http://arc.aiaa.org | DOI: 10.2514/1.J056482